The ratio of transverse to longitudinal turbulent velocity statistics for aircraft measurements

Jakub L. Nowak[1], Marie Lothon[2], Donald H. Lenschow[3], and Szymon P. Malinowski[1]

[1]Institute of Geophysics, Faculty of Physics, University of Warsaw, Warsaw, Poland
[2]Laboratoire d'Aérologie, University of Toulouse, CNRS, UPS, Toulouse, France
[3]National Science Foundation National Center for Atmospheric Research, Boulder, CO, USA

Correspondence: Jakub L. Nowak (jakub.nowak@fuw.edu.pl)

Abstract. The classical theory of homogeneous isotropic turbulence predicts the ratio of transverse to longitudinal structure functions or power spectra equal to 4/3 in the inertial subrange. For the typical turbulence cascade in the inertial subrange, it also predicts a power law scaling with an exponent of +2/3 and -5/3 for the structure functions and the power spectra, respectively.

5   We estimate those ratios and exponents from in-situ high-rate turbulence measurements collected by three research aircraft during four field experiments in two regimes of the marine atmospheric boundary layer: shallow trade-wind convection and subtropical stratocumulus. The results were derived by fitting power law formulas to the structure functions and power spectra computed separately for the three components of the turbulent wind velocity measured in horizontal flight segments.

The variability in the results can be attributed to how the wind velocity components are measured on an individual aircraft.
10   The differences related to environmental conditions, e.g. between characteristic levels and regimes of the boundary layer, are of secondary importance. Experiment-averaged transverse-to-longitudinal ratios are 23-46 % smaller than predicted by the theory. The deviations of average scaling exponents with respect to the theoretical values range from -35 to +47 % for structure functions and from -25 to +22 % for power spectra, depending on experiment and velocity component. The reason for the disagreement in transverse-to-longitudinal ratios between the observations and the theory remains uncertain.

15 1   Introduction

Turbulent fluctuations of wind velocity far from the surface are typically measured in-situ from research aircraft in the course of intensive field experiments (e.g. Nicholls, 1984; Duynkerke et al., 1995; Lenschow et al., 2000; Malinowski et al., 2013; Brilouet et al., 2021). Many of the subsequent analyses utilize mostly the vertical velocity measurements to calculate variance and turbulent fluxes (e.g. Nicholls and Leighton, 1986; Tjernström and Rogers, 1996; Faloona et al., 2005; Zheng et al., 2011),
20   which are of primary interest for the structure of the atmospheric boundary layer (ABL) as well as for heat and moisture transport (Stull, 1988). Others estimate turbulence kinetic energy dissipation rate ϵ, which is considered as a practical measure of turbulence intensity and as an important parameter for cloud microphysics (Grabowski and Wang, 2013) and turbulence parameterization in mesoscale or global models (Mauritsen et al., 2007).

Research aircraft capable of turbulence measurements are often equipped with a five-hole radome probe with pressure transducers and a Pitot tube for air velocity measurements, and an inertial navigation system coupled to a GPS unit. The three components of the wind velocity are computed by adding the aircraft velocity with respect to the earth and the velocity of air with respect to the aircraft which is inferred from true air speed (TAS), and attack and sideslip angles (Brown et al., 1983; Lenschow, 1986; Lenschow and Spyers-Duran, 1989). TAS is obtained from the measurements of total and static pressure whereas attack and sideslip angles are determined from the differential pressure between vertically and horizontally aligned ports of the five-hole probe, respectively. This technique requires careful calibration for each specific aircraft which is carried out using a series of calibration maneuvers (Lenschow and Spyers-Duran, 1989). For a typical TAS of about $100\,\mathrm{m\,s^{-1}}$ and a sampling rate of a few tens of Hz, commonly used instruments provide spatial resolution of a few meters. A few studies applied fast-response hot-wire or hot-film anemometers to reach better resolution (Sheih et al., 1971; Merceret, 1976a, b; Lenschow et al., 1978) but ensuring the long-term maintenance of those instruments is more difficult. Ultrasonic and hot-wire anemometers are typically used on helicopter, UAV or tethered balloon platforms (Siebert and Muschinski, 2001; Siebert et al., 2006a, 2007).

As a consequence, the dissipative scales (of the order of millimeters) are hardly resolved in aircraft measurements which prevents direct application of the microscopic definition of ϵ (e.g. Pope, 2000, ch. 5). Instead, the universal scaling of the turbulent velocity statistics in the resolved inertial subrange predicted by the Kolmogorov theory (Kolmogorov, 1941) is often exploited in practice to derive ϵ from moderate resolution airborne measurements (e.g. Lambert and Durand, 1999; Siebert et al., 2006b; Jen-La Plante et al., 2016; Wacławczyk et al., 2020). In such an approach, the assumptions of the theory, including local isotropy and homogeneity, are taken for granted even though in the atmosphere there are directions naturally distinguished in larger scales due to buoyancy and wind shear (e.g. Lenschow, 1974; Darbieu et al., 2015).

According to the theory of homogeneous isotropic turbulence formulated by Kolmogorov, which is introduced in many classical textbooks (e.g. Pope, 2000, ch. 6), the second-order longitudinal and transverse velocity structure functions in the inertial subrange can be approximated to

$$D_L(r) = B_L(\epsilon r)^{2/3}, \quad D_T(r) = B_T(\epsilon r)^{2/3}, \tag{1}$$

respectively, where r is the separation distance, ϵ is the turbulence kinetic energy dissipation rate and B_L, B_T are constants. Due to isotropy and homogeneity, the ratio of those structure functions is

$$\frac{D_T}{D_L} = \frac{4}{3}. \tag{2}$$

Analogous to structure functions, one-dimensional longitudinal and transverse velocity power spectra in the inertial subrange are

$$P_L(k) = C_L \epsilon^{2/3} k^{-5/3}, \quad P_T(k) = C_T \epsilon^{2/3} k^{-5/3}, \tag{3}$$

respectively, where k is the longitudinal wavenumber, C_L, C_T are constants and

$$\frac{P_T}{P_L} = \frac{4}{3}. \tag{4}$$

Only one of the four constants needs to be determined experimentally, as due to isotropy they are functionally related. The approximate values are $B_L \approx 2.0$, $B_T \approx 2.6$, $C_L \approx 0.49$, $C_T \approx 0.65$ (e.g. Saddoughi and Veeravalli, 1994; Sreenivasan, 1995).

Kolmogorov did not specify precise limits for the applicability of his theory. Instead, his famous hypotheses state that sufficiently far from the boundaries and for sufficiently large Reynolds number, there exist a range of scales where the turbulent velocity statistics are isotropic and universal. Nevertheless, the simplicity of this theory is considered as advantageous in experimental practice, despite some recent theoretical advancements examining non-stationary, non-homogeneous or non-isotropic conditions (e.g. Gomes-Fernandes et al., 2015; Wacławczyk et al., 2022).

The local isotropy hypothesis has been extensively tested in wind tunnels (e.g. Saddoughi and Veeravalli, 1994) and with ground-based measurements in the atmospheric surface layer (e.g. Kaimal et al., 1972; Chamecki and Dias, 2004). Far from the surface, it is generally more challenging. A few analyses have attempted to consider the limitations of the theory, for example by comparing the estimates of ϵ derived from the three velocity components independently (e.g. Jen-La Plante et al., 2016; Nowak et al., 2021). Lothon and Lenschow (2005a, 2007) reported P_T/P_L close to 1 instead of the theoretical 4/3 in DYCOMS-II experiment (Stevens et al., 2003) made with the NSF/NCAR C130 research aircraft (Earth Observing Laboratory) in marine stratocumulus. Lothon and Lenschow (2005b) extended this analysis for several other field experiments made with the same aircraft - GOTEX (Romero and Melville, 2010), IDEAS (Stith and Rogers, 2004), RICO (Rauber et al., 2007b), EPIC (Raymond et al., 2004) - which covered marine and continental boundary layers, with stratocumulus, cumulus or clear sky conditions. They found P_T/P_L equal to about 0.8 on average. After applying a correction for the upwash distortion, the vertical-to-longitudinal ratio became close to 4/3 in average. However, this correction does not impact the lateral-to-longitudinal ratio which then remained approximately 0.8. On the other hand, Siebert et al. (2006b) confirmed the approximate 4/3 value of P_T/P_L in their helicopter-borne measurements in cumulus clouds. With a bit different approach, Pedersen et al. (2018) considered the scale-by-scale ratio of horizontal-to-vertical velocity spectra below stratocumulus top. They found strong scale dependence, with average close to 1 at wavelengths smaller than the ABL depth and horizontal-to-vertical ratios ranging from about 1 to 10 at higher wavelengths (see Fig. 2 therein). Nevertheless, there are still rather few works investigating the proportion between transverse and longitudinal velocity statistics in airborne measurements in the ABL; likely because most estimates of the dissipation rate have been obtained from one wind velocity component only.

Likewise, the scaling exponents in the inertial subrange have not been extensively investigated experimentally in the ABL. Lothon and Lenschow (2005a, 2007, 2005b) reported an average vertical velocity spectrum exponent of about -2 instead of the theoretical -5/3 in the five field experiments mentioned above. However, as a result of their upwash correction, it became approximately -1.5. The exponents for the lateral and longitudinal velocity spectra averaged about -1.8 and -1.5, respectively. Darbieu et al. (2015) studied the evolution of vertical velocity spectra in turbulence decay during afternoon transition. They observed the slopes of the spectra steeper than theoretical in the fully convective phase which they potentially related to the role of coherent convective structures and associated anisotropy. On the other hand, they found the slopes gradually flatten during afternoon transition to become considerably flatter than the theoretical around sunset. Nowak et al. (2021) analyzed measurements obtained with a helicopter-borne platform in the marine stratocumulus-topped boundary layer. They found

90 exponents for both structure functions and power spectra relatively close to the theory in coupled stratocumulus but significantly smaller in absolute values and highly variable with altitude in the decoupled case.

The inspiration for this study originates from the surprising results we encountered while analyzing the dissipation rates derived independently from three wind velocity components measured by an aircraft in a trade-wind ABL. This motivated us to generalize our analysis by focusing on the transverse-to-longitudinal ratio and on the scaling of second order velocity

95 statistics, and by considering other aircraft participating in other field campaigns. Therefore, here we compare the observed ratio of transverse and longitudinal statistics (structure functions and power spectra) in the inertial subrange with the theoretical value of 4/3. Secondly, we compare the observed scaling of structure functions and power spectra with the theoretical exponents of 2/3 and -5/3, respectively. For this purpose, we use open datasets for four field experiments involving three different aircraft.

The paper is structured as follows. Sec. 2 introduces the measurements of turbulence collected during four field experiments

100 together with the available datasets and explains the selection of data for our study. Sec. 3 describes the methods used to derive the relevant parameters. Sec. 4 presents the results on the transverse-to-longitudinal ratio and inertial subrange scaling, and compares them with the theoretical predictions. Sec. 5 discusses the possible reasons and consequences of the observed departure from theoretical values. Finally, our findings are summarized in the last section.

2 Observations

2.1 Field experiments

The measurements considered in this study were performed during four field experiments:

- EUREC4A (Elucidating the role of cloud–circulation coupling in climate) in Jan - Feb 2020 in trade-wind cumulus regime in northwestern Atlantic (Stevens et al., 2021),

- RICO (Rain in Cumulus Over Ocean) in Nov 2004 - Jan 2005 in trade-wind cumulus regime in northwestern Atlantic

110 (Rauber et al., 2007b),

- VOCALS-REx (Variability of the American Monsoon Systems Ocean-Cloud-Atmosphere-Land Study Regional Experiment) in Oct-Nov 2008 in subtropical stratocumulus regime in southeastern Pacific (Wood et al., 2011),

- POST (Physics of the Stratocumulus Top) in Jul-Aug 2008 in subtropical stratocumulus regime in northeastern Pacific (Carman et al., 2012; Malinowski et al., 2013; Gerber et al., 2013).

115 The objectives, strategy and execution of the experiments are described in the references given above. EUREC4A addressed many research questions comprising atmospheric circulation, clouds, rain formation, life cycle of particulate matter, upper-ocean processes and air-sea interaction. The meteorological conditions and the structure of the ABL observed during EUREC4A are analyzed in detail by Albright et al. (2022). RICO investigated the mechanism of rain formation in shallow cumuli and its feedback on the structure and variability of those clouds. VOCALS-REx studied interactions between aerosols, mi-

120 crophysics, precipitation and radiation in marine stratocumulus as well as physical and chemical couplings between the upper

ocean and the lower atmosphere in the region of one of the strongest coastal upwelling. POST focused particularly on processes occurring at the interface between the stratocumulus-topped ABL and the free troposphere.

2.2 Aircraft

The turbulence measurements in the ABL analyzed here were obtained with three research aircraft:

125 – SAFIRE (the French facility for airborne research) ATR42 (SAFIRE) during EUREC4A,

– NSF/NCAR (National Science Foundation - National Center for Atmospheric Research) C130 (Earth Observing Laboratory) during RICO and VOCALS-REx,

– NPS CIRPAS (Naval Postgraduate School - Center for Interdisciplinary Remotely-Piloted Aircraft Studies) Twin Otter (TO; NASA Airborne Science Program) during POST.

130 The three aircraft are equipped with a five-hole radome probe and the three components of turbulent wind velocity are computed similar to the methods described by Lenschow (1986). The aircraft differ in size and cruising speed. The C130, ATR and TO feature wing span of about 40, 25 and 20 m, respectively. The typical TAS of the ATR and C130 is $\sim 100\,\mathrm{m\,s^{-1}}$ which with the sampling rate $f_s = 25\,\mathrm{Hz}$ provides a spatial resolution $\Delta r = TAS/f_s \sim 4\,\mathrm{m}$. The typical TAS of the TO is $\sim 55\,\mathrm{m\,s^{-1}}$ which with $f_s = 40\,\mathrm{Hz}$ gives a resolution $\Delta r \sim 1.4\,\mathrm{m}$. For the ATR during EUREC4A, the instrumentation and sampling 135 strategy are described in Bony et al. (2022) while the turbulence measurements are described in Brilouet et al. (2021).

2.3 Datasets

The turbulence data for the four experiments were downloaded from public datasets (Lothon and Brilouet, 2020; UCAR/NCAR - Earth Observing Laboratory, 2011a, b; Khelif, 2009, for EUREC4A, RICO, VOCALS-REx and POST, respectively). Wind velocity is reported there with the use of the vertical component w and the two horizontal components. The datasets 140 related to EUREC4A, RICO and VOCALS-REx already contain longitudinal u and lateral v (with respect to the aircraft) wind velocity components. For POST, we computed them by rotating eastward and northward components into the aircraft oriented coordinate system. Note that both vertical and lateral wind components are considered transverse.

2.4 Flight segments

We analyze only horizontal flight segments in the ABL. The fixed flight pattern during EUREC4A included straight horizontal 145 segments at four levels: close to the cloud base, near the top of the subcloud layer, in the middle of the subcloud layer and near the surface; in the direction either parallel or perpendicular to the mean wind. During RICO, the flights included horizontal circles ($\sim 60\,\mathrm{km}$ diameter) above the surface and below the cloud base as well as straight horizontal segments at various heights in the subcloud and cloud layers. In VOCALS-REx, the flights included straight horizontal segments mostly at $\sim 100\,\mathrm{m}$ or inside the cloud. During POST, the flights included straight horizontal segments typically at three levels in the ABL: close 150 to the cloud top, near the cloud base and near the surface.

For EUREC4A, we applied the definition of segments and their classification according to level (*cloud-base, top-subcloud, mid-subcloud, near-surface*) from the same dataset as turbulence records (Lothon and Brilouet, 2020). In the case of VOCALS-REx, we used segment timestamps and levels (*in-cloud, cloud-base, sub-cloud*) from the related dataset devoted to lidar measurements (Leon et al., 2011).

155 For RICO and POST, no a priori segment information is available which is why we developed our own segmentation algorithm based on the conditions of small derivatives of altitude and true heading with respect to distance (see Appendix A). We also crudely classified the detected segments according to characteristic levels. The classification is only approximate as the detailed characterization of ABL stratification in each of the flights is beyond the scope of this study. In the case of RICO, we marked the segments below $990\,\mathrm{hPa}$ as *near-surface*, others below $950\,\mathrm{hPa}$ as *sub-cloud*, others below $900\,\mathrm{hPa}$ as *cloud-*

160 *base*, others below $800\,\mathrm{hPa}$ as *cloud-layer*, following Fig. 5 of Rauber et al. (2007b). For POST, we exploited the information on average cloud base height, average cloud top height and standard deviation of cloud top height for each flight collected in Table 1 of Carman et al. (2012). The segments below $60\,\mathrm{m}$ were marked as *near-surface*, others below the cloud base as *sub-cloud*, others below the cloud middle as *cloud-base*, others below the average cloud top height plus its one standard deviation as *cloud-top*.

165 Brilouet et al. (2021) report several technical difficulties encountered during EUREC4A, e.g. concerning one of the radome transducers in flights RF02 to RF08 and the failure of inertial navigation in RF20, and conclude that flights RF09 to RF19 had much better-quality data. For this reason, we considered those 11 flights only. From other experiments, we used all flights available in the datasets.

The segment number, average altitude and length for each experiment and level are summarized in Table 1. In EUREC4A

170 and POST, most of the segments were flown either along or across the mean wind direction. Hence, we distinguish them in the following figures by filled and open symbols, respectively.

3   Analysis

The lateral-to-longitudinal D_v/D_u and vertical-to-longitudinal D_w/D_u ratios of structure functions, and the analogous ratios of power spectral densities P_v/P_u, P_w/P_u for each segment were calculated with the methods similar to those used in sec. 4.3

175 of Nowak et al. (2021) to estimate dissipation rates.

Structure functions D_i computed for each velocity component $i = u, v, w$ (longitudinal, lateral and vertical, respectively) from linearly detrended records were averaged in 5 logarithmically equidistant bins covering the selected fitting range (defined further). The ratios were obtained by dividing adequate prefactors B_i resulting from the least-squares fit of the relationship

$$D_i(r) = B_i r^{2/3}, \tag{5}$$

180 where r is the separation distance.

Power spectral densities P_i were computed from linearly detrended velocity records using the Welch algorithm (Welch, 1967) with window length of $1\,\mathrm{km}$ and window overlap of $0.5\,\mathrm{km}$. Similarly to D_i, they were averaged in 5 logarithmically

Table 1. Statistics of the segments considered in the analysis: number of segments at each level, average altitude, length and integral length scale for vertical wind velocity (defined in sec. 3). Standard deviations are given in parentheses.

Level	Number	Altitude [m]	Integral scale [m]	Length [km]
ATR-EUREC4A				
cloud-base	116	806 (83)	267 (136)	54 (5)
top-subcloud	20	592 (45)	246 (109)	62 (10)
mid-subcloud	19	291 (26)	195 (77)	56 (9)
near-surface	10	64 (3)	58 (30)	41 (6)
C130-RICO				
cloud-layer	53	1547 (296)	258 (224)	50 (17)
cloud-base	51	804 (114)	164 (144)	48 (16)
sub-cloud	49	399 (70)	152 (97)	154 (72)
near-surface	55	97 (28)	81 (23)	136 (72)
C130-VOCALS				
in-cloud	88	1156 (265)	100 (29)	80 (44)
cloud-base	6	570 (216)	214 (135)	176 (52)
sub-cloud	84	148 (14)	95 (17)	76 (44)
TO-POST				
cloud-top	44	410 (124)	123 (116)	27 (7)
cloud-base	22	271 (102)	95 (57)	31 (16)
sub-cloud	44	176 (122)	64 (100)	26 (8)
near-surface	49	32 (6)	13 (4)	24 (6)

equidistant bins covering the fitting range and the ratios were obtained by dividing adequate prefactors C_i resulting from the least-squares fit of the relationship

185 $$P_i(f) = C_i f^{-5/3} \tag{6}$$

where f is frequency.

7

In addition, we evaluated the scaling exponents of structure functions s_i and power spectra p_i with separate least-squares fits of the formulas

$$D_i(r) = B_i^* r^s \tag{7}$$

190
$$P_i(f) = C_i^* f^{-p} \tag{8}$$

performed on the same averaged points as before. The parameters B_i^*, C_i^* are not used in further analysis. The estimation of the uncertainties of the computed transverse-to-longitudinal ratios and scaling exponents is discussed in Appendix B.

The choice of the fitting range was guided by the spatial resolution of measurements (see sec. 2.2), integral length scale for the vertical velocity (given in Table 1) and the manual inspection of the observed extension of power-law scaling, in particular

195 for the segments at the lowest levels. The integral length scale L was estimated as the distance at which the autocorrelation function of vertical velocity declines by a factor of e (c.f. Nowak et al., 2021, sec. 4.5). We observed that the power-law typically extends to the scales larger than such an estimation of the integral length scale.

Examples of our fitting procedure are illustrated in Fig. 1 and 2 for structure functions and power spectra, respectively. In the case of EUREC4A, RICO and VOCALS-REx, we applied the fitting ranges $[2\Delta r, L]$ for D_i and $[4\Delta r, 2L]$ for P_i. The

200 lower ends correspond to twice the smallest r and twice the Nyquist frequency, respectively. For POST, we applied the ranges of $[3\Delta r, L]$ and $[6\Delta r, 2L]$ in order to avoid the influence of a spurious peak at $\sim 5.5\,\mathrm{m}$ corresponding to the frequency of $\sim 10\,\mathrm{Hz}$ which is symptomatic for most of the segments (c.f. Fig. 2). The sensitivity of the results to the choice of the fitting range is discussed in Appendix C.

The different fitting ranges for D_i and P_i are used here following the remarks given by Chamecki and Dias (2004) and

205 Wacławczyk et al. (2020). The former found a shorter extension of the inertial subrange in the structure functions in comparison with the power spectra (which manifests in diverging ratios D_T/D_L and P_T/P_L). The latter derived ϵ with inertial scaling methods and found the best agreement with reference ϵ for the structure function fitting range moved towards smaller scales in comparison with the fitting range for power spectra.

4 Results

210 The lateral-to-longitudinal ratios D_v/D_u, P_v/P_u are presented in Fig. 3. In general, most of the points cluster in the vicinity of the value of 3/4 for both ratios, in particular in the case of EUREC4A. This stands in striking contrast with 4/3 predicted for homogeneous isotropic turbulence. The largest variability is observed for POST, the smallest for EUREC4A. The former is supposedly connected with the segment lengths shorter than for other experiment which increases random error (c.f. Lenschow et al., 1994, Eq. (36)), relatively shallow ABL depth and strong wind shear at cloud top (Carman et al., 2012; Malinowski et al.,

215 2013; Jen-La Plante et al., 2016). Nevertheless, D_v/D_u and P_v/P_u approximately agree with each other in all the experiments. There are only minor differences between the levels within the experiments, see the average values reported in Table 2. The level averages range from 0.67 to 0.97. The experiment averages range from 0.72 to 0.94 which is 30-46 % smaller than the
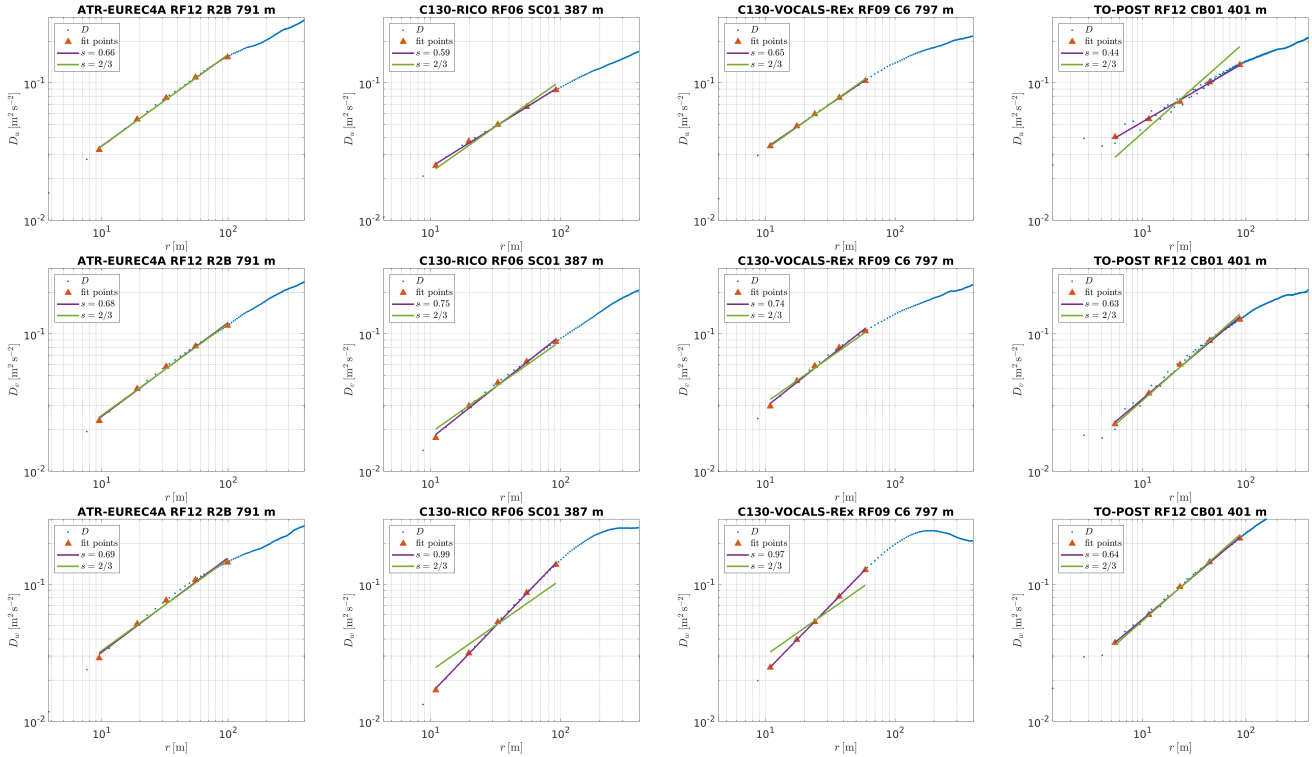
Figure 1. Examples of structure functions (blue points) and the fitting procedure performed on the averaged logarithmically spaced points (red triangles). The green and purple line are best fits of Eq. (5) and (7), respectively. The aircraft, experiment, flight, segment name and segment altitude are given in panel titles.

theoretical value. The experiment-averaged lateral-to-longitudinal ratio is the largest for VOCALS-REx and the smallest for POST. The average P_v/P_u are roughly in agreement with Lothon and Lenschow (2005b) for all the experiments and levels.

220   The vertical-to-longitudinal ratios D_w/D_u, P_w/P_u are shown in Fig. 4. Almost all of the points are far from the predicted 4/3 value. The largest variability is observed for POST and RICO, the smallest for EUREC4A. In contrast to the lateral-to-longitudinal ratios, the differences between the aircraft are more significant. Apart from distinct variability, there is little difference between RICO and VOCALS-REx which both involved the C130. For EUREC4A and POST, D_w/D_u approximately agrees with P_w/P_u. For RICO and VOCALS-REx, D_w/D_u is systematically higher than P_w/P_u. There are also some

225 variations between the levels (see the averages given in Table 2), possibly due to the impact of buoyancy or mean wind shear (c.f. Darbieu et al., 2015; Pedersen et al., 2018). For example, on average the mid-subcloud level exhibits higher ratios than other levels for EUREC4A while the near-surface level is characterized by lower ratios than cloud levels for POST and RICO. The level averages range from 0.80 to 1.11 for D_w/D_u and from 0.64 to 1.06 for P_w/P_u which is 16-40 % and 20-52 % smaller than the theoretical value.
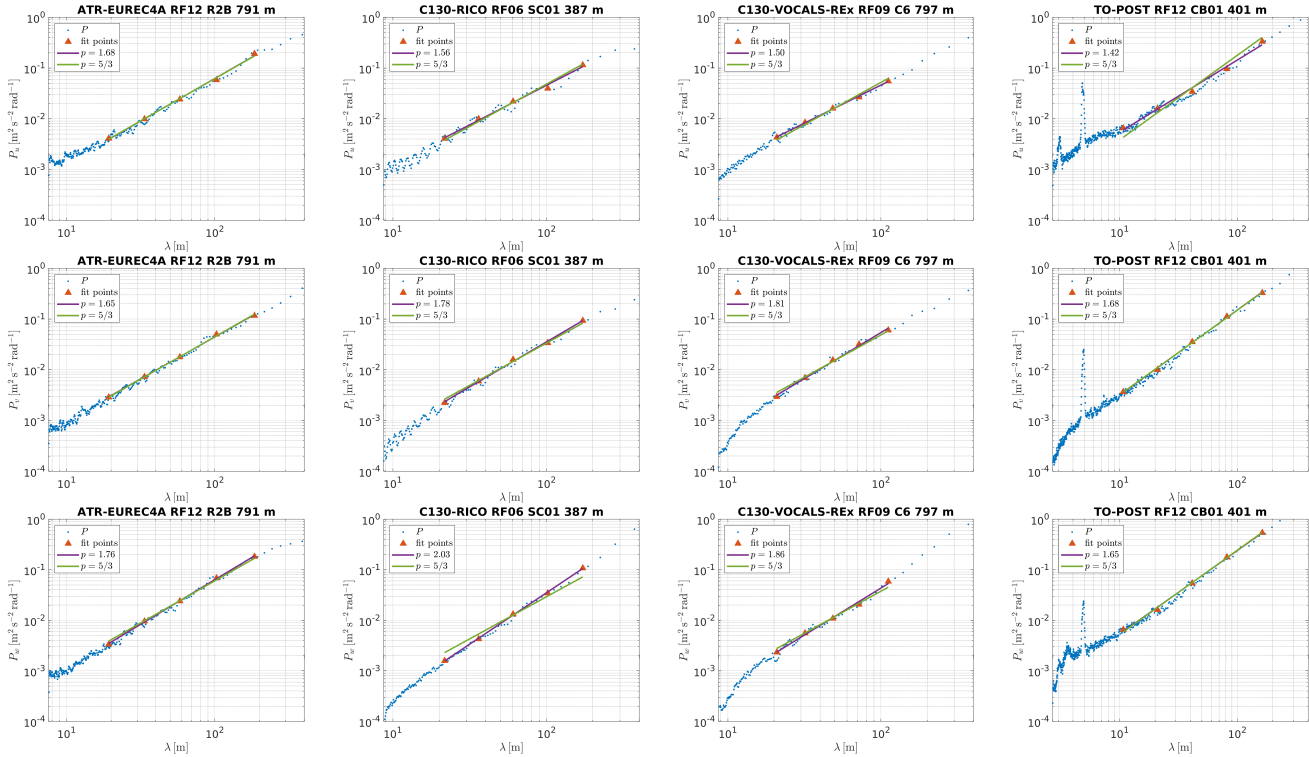
Figure 2. Examples of power spectral densities (blue points) and the fitting procedure performed on the averaged logarithmically spaced points (red triangles). The green and purple line are best fits of Eq. (6) and (8), respectively. The aircraft, experiment, flight, segment name and segment altitude are given in panel titles. The spectral density is in practice computed with respect to normalized angular frequency, hence the units. Note the orientation of the horizontal axis providing wavelengths λ is opposite to a typical presentation of a spectrum for the sake of easy comparison with the structure functions given in Fig. 1.

230   Fig. 5 presents the exponents s and p. The points are dispersed in the neighborhood of the predicted $s = 2/3$ and $p = 5/3$. There are considerable differences between velocity components. The clusters of points representing the longitudinal component are almost separated from those for the transverse components in the case of RICO, VOCALS-REx and POST. The differences related to the aircraft are also visible. The variations among the levels within the experiments are rather minor. Hence, we report the average values for entire experiments in Table 3. The experiment-averaged structure functions exponents

235   can be from 0.43 for s_u to 0.98 for s_w, i.e. 35 % lower and 47 % higher than the predicted 2/3. The experiment-averaged power spectra exponents take values from 1.24 for p_u to 2.03 for p_w which is 25 % lower and 22 % higher than 5/3. Particularly close to the theoretical predictions are the average exponents for EUREC4A, s_u for RICO as well as s_v and p_v for POST. For RICO and VOCALS, average p_w is close to 2 in agreement with the results of Lothon and Lenschow (2005a, b, 2007) before applying their upwash correction.
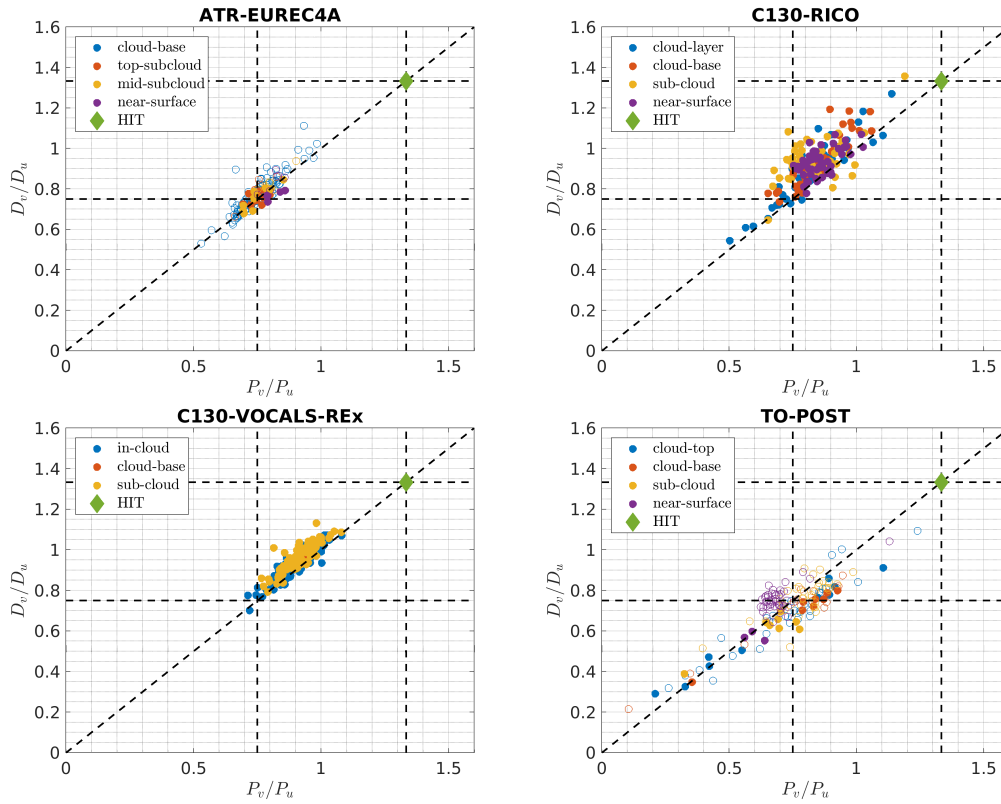
Figure 3. The lateral-to-longitudinal ratios of structure functions with respect to the analogous ratios of power spectra. Each circle denotes one segment. For EUREC4A and POST, filled and open symbols correspond to the segments flown parallel and perpendicular to the mean wind direction, respectively. Colors denote characteristic levels of the boundary layer (see sec. 2.4 and Table 1). Horizontal and vertical black dashed lines mark the values of 4/3 and 3/4. Diagonal black dashed line denotes 1:1 proportion. The green diamond shows the theoretical prediction for homogeneous isotropic turbulence (HIT).

5 Discussion

The results of our analysis suggest that the variability in the transverse-to-longitudinal ratios and scaling exponents of velocity statistics can be attributed to how the velocity components are measured on the aircraft. The differences between field experiments and ABL levels seem to be of secondary importance. This motivates an examination of the details of measurement technique and instrument properties.

In general, airborne measurements suffer from errors which are often challenging to quantify because of flow distortion induced by the airplane (Wendisch and Brenguier, 2013). Rauber et al. (2007a) reported that velocity measurements on the C130 during RICO showed attenuation at high frequencies for v and w. The measurements for VOCALS-REx probably suffered from the same issue. This can be spotted in the spectra in Fig. 2 which are representative of most of the segments. In contrast to Rauber et al. (2007a), we observe w to be more affected than v. A similar problem is evident for the TO during POST. In ad-

11

Table 2. Average values of the ratios of structure functions and power spectra. Standard deviations are given in parentheses.

Aircraft/Campaign	D_v/D_u	P_v/P_u	D_w/D_u	P_w/P_u
ATR-EUREC4A				
cloud-base	0.77 (0.09)	0.75 (0.08)	0.87 (0.11)	0.87 (0.12)
top-subcloud	0.77 (0.05)	0.75 (0.04)	0.88 (0.10)	0.87 (0.10)
mid-subcloud	0.78 (0.06)	0.77 (0.05)	0.98 (0.08)	0.95 (0.05)
near-surface	0.80 (0.05)	0.81 (0.03)	0.84 (0.05)	0.88 (0.05)
all	0.78 (0.08)	0.76 (0.07)	0.88 (0.10)	0.88 (0.11)
C130-RICO				
cloud-layer	0.89 (0.14)	0.82 (0.12)	1.11 (0.28)	0.84 (0.19)
cloud-base	0.93 (0.12)	0.85 (0.09)	1.11 (0.15)	0.88 (0.11)
sub-cloud	0.95 (0.10)	0.84 (0.10)	0.97 (0.15)	0.64 (0.12)
near-surface	0.93 (0.06)	0.85 (0.06)	0.91 (0.12)	0.68 (0.10)
all	0.92 (0.11)	0.84 (0.10)	1.02 (0.21)	0.76 (0.17)
C130-VOCALS				
in-cloud	0.91 (0.07)	0.89 (0.07)	0.95 (0.13)	0.77 (0.08)
cloud-base	0.97 (0.03)	0.94 (0.04)	0.91 (0.13)	0.81 (0.11)
sub-cloud	0.96 (0.07)	0.91 (0.06)	0.92 (0.12)	0.75 (0.06)
all	0.94 (0.07)	0.90 (0.07)	0.94 (0.13)	0.76 (0.07)
TO-POST				
cloud-top	0.67 (0.19)	0.72 (0.23)	0.95 (0.32)	1.02 (0.38)
cloud-base	0.70 (0.17)	0.76 (0.22)	0.97 (0.21)	1.06 (0.28)
sub-cloud	0.74 (0.11)	0.77 (0.12)	0.90 (0.13)	1.03 (0.14)
near-surface	0.75 (0.08)	0.68 (0.08)	0.80 (0.09)	0.85 (0.09)
all	0.72 (0.14)	0.73 (0.17)	0.89 (0.21)	0.98 (0.25)

250 dition, the POST spectra exhibit a pronounced peak at $\sim 5.5\,\mathrm{m}$ corresponding to a frequency of $\sim 10\,\mathrm{Hz}$ which is symptomatic for most of the segments. The peak may have resulted from an internal resonance of measurement system (Djamal Khelif, personal communication). However, this effect influences the wavelengths outside our fitting range, so it does not explain the results, in particular the departure of the transverse-to-longitudinal ratios from the predicted 4/3.

D_w/D_u and P_w/P_u might possibly be affected by the conditions violating the isotropy assumption, e.g. due to buoyancy.

255 The substantial deviations of D_v/D_u, P_v/P_u from 4/3 are hardly possible to justify either with instrumental factors or boundary
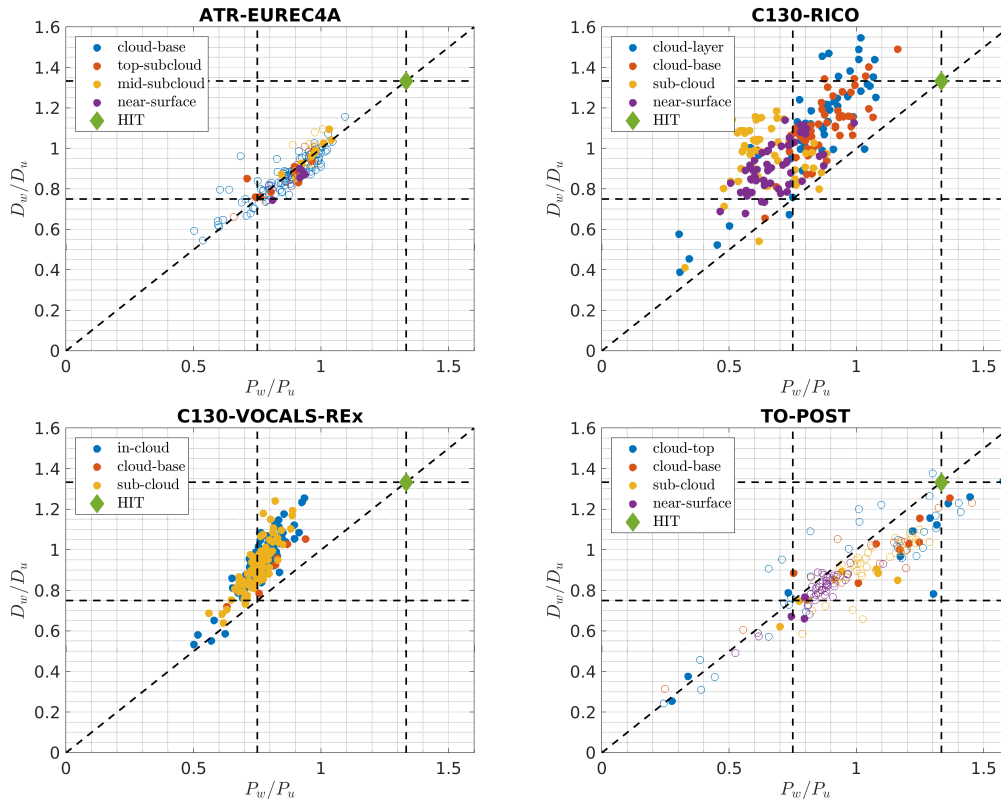
Figure 4. As in Fig. 3 but for the vertical-to-longitudinal ratios. One point for RICO (in cloud layer) and one point for POST (at cloud top) lie outside the range presented here.

Table 3. Average values of the scaling exponents of structure functions and power spectra. Standard deviations are given in parentheses.

Aircraft/Campaign	s_u	s_v	s_w	p_u	p_v	p_w
ATR-EUREC4A	0.67 (0.05)	0.72 (0.07)	0.69 (0.07)	1.66 (0.11)	1.68 (0.11)	1.71 (0.08)
C130-RICO	0.64 (0.06)	0.80 (0.07)	0.98 (0.11)	1.55 (0.10)	1.78 (0.08)	2.03 (0.13)
C130-VOCALS	0.62 (0.04)	0.75 (0.04)	0.93 (0.08)	1.51 (0.06)	1.80 (0.06)	1.93 (0.09)
TO-POST	0.43 (0.07)	0.70 (0.13)	0.58 (0.10)	1.25 (0.17)	1.65 (0.14)	1.53 (0.19)

conditions as they exist even in the interior (far from the surface and top) of well-mixed ABL. Note that the uncertainties are also smaller than those deviations, see Appendix B.

Consequently, the reason for the disagreement between the observations and the theory remains uncertain. We presume that potential explanations might be: the inapplicability of the Kolmogorov theory for the conditions present in ABL which may depart from isotropy and homogeneity, the uncertain influence of the flow around an airplane (e.g. upwash effect) which has
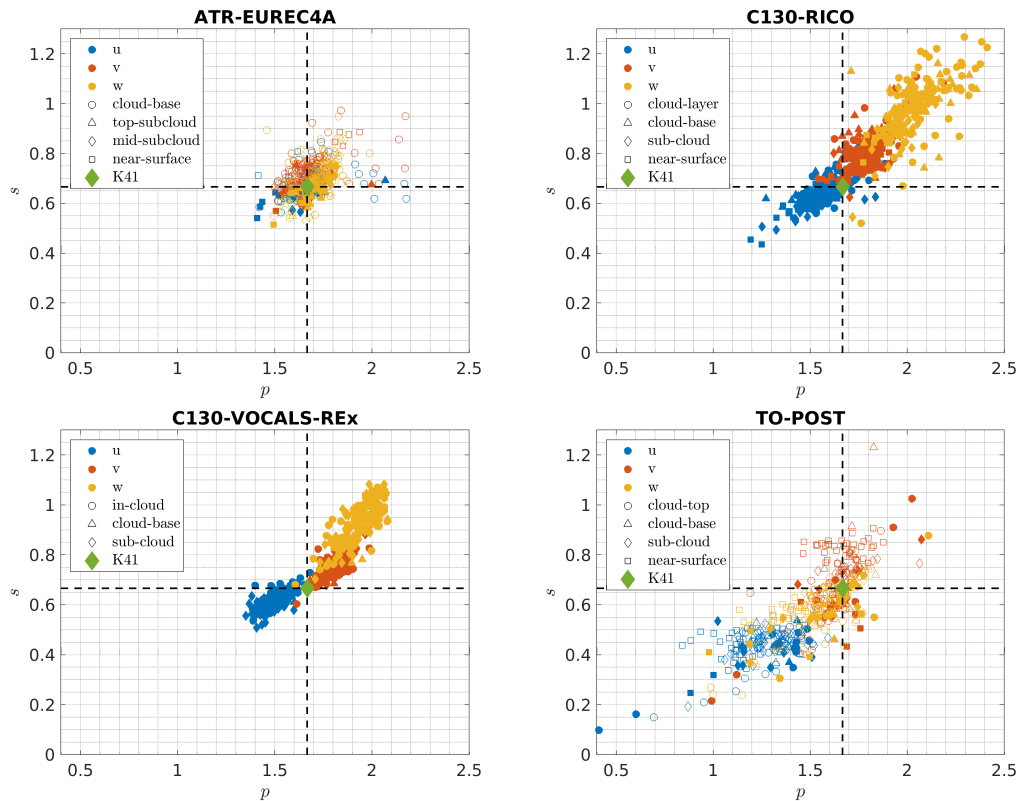
260

13

Figure 5. The exponents of structure functions s with respect to the exponents of power spectra p. Each circle denotes one segment. For EUREC4A and POST, filled and open symbols correspond to the segments flown parallel and perpendicular to the mean wind direction, respectively. Colors denote velocity components while different symbols denote characteristic levels of the boundary layer (see sec. 2.4 and Table 1). Black dashed lines mark the theoretical values of 2/3 and 5/3. The green diamond shows the prediction of the Kolmogorov theory (K41).

finite mass and complex geometry, and shortcomings of the instrumental systems that measure pressure differences in a five-hole probe. This question deserves attention and further investigation. This would likely help us improve our measurements of turbulence and our understanding of boundary layer turbulence.

6 Summary and conclusions

265 The classical theory of homogeneous isotropic turbulence predicts the ratios of transverse to longitudinal second order velocity structure functions and power spectra are 4/3 in the inertial subrange. In the inertial subrange, those statistics should exhibit power-law scaling with an exponent of +2/3 and -5/3 for the structure functions and power spectra, respectively.

We studied the transverse-to-longitudinal ratios and scaling exponents derived from in-situ measurements performed by three research aircraft (SAFIRE ATR42, NSF/NCAR C130, CIRPAS Twin Otter), all equipped with a high-rate five-hole radome

270 probe, during four field experiments (EUREC4A, RICO, VOCALS-REx, POST) in two regimes of the marine atmospheric boundary layer (shallow trade-wind convection and subtropical stratocumulus).

The observed lateral-to-longitudinal ratios D_v/D_u, P_v/P_u significantly depart from the theoretical value. The experiment-averaged values are from 0.72 to 0.94 which is 30-46 % smaller than predicted. The differences between the levels of the ABL are hardly noticeable. There is a good agreement of D_v/D_u with P_v/P_u.

275 The vertical-to-longitudinal ratios D_w/D_v, P_w/P_u exhibit higher variability. They also depart from 4/3. There are significant differences between the aircraft and some noticeable variations between the characteristic levels. Despite different ABL regime, there is little difference between RICO and VOCALS-REx which both involved C130. The level averages are from 0.64 to 1.11 which is 16-52 % smaller than predicted.

On the other hand, the scaling exponents s and p are for the most part distributed around Kolmogorov's 2/3 and 5/3 power law
280 exponents, respectively. The experiment averages differ from the predicted values by -35 to +47 % for structure functions and by -25 to +22 % for power spectra. There are significant differences between aircraft, and between longitudinal and transverse wind velocity components. The variations among the levels are minor. The results for RICO and VOCALS-REx are similar in spite of different ABL regime.

In general, our results suggest that the variability in the transverse-to-longitudinal ratios and scaling exponents can be
285 attributed to how the velocity components are measured on the aircraft. The differences between field experiments, representing different ABL regimes, and between ABL levels are of secondary importance. The explanation of the large departures of the transverse-to-longitudinal ratio from 4/3 remains uncertain. This issue warrants further investigation as it is currently a major impediment in using aircraft measurements to study the structure of atmospheric turbulence.

In particular, the documented departure of the transverse-to-longitudinal ratio from the predicted isotropic value directly
290 relates to the disparate estimates of dissipation rate obtained separately for three wind velocity components using the universal scaling as in Eqs. (1) and (3). We suggest a way to solve this problem might be to carry out a study of the turbulence energy budget throughout the ABL with an airplane equipped with the radome-based measuring system using a flight and analysis strategy similar to that used by Lenschow (1974). This would be best carried out over a flat homogeneous surface in a situation of strong surface heating and light wind to maximize the ratio of buoyancy production of turbulence to shear production. By
295 flying a series of horizontal flight legs at several levels throughout the ABL, the total production of turbulence within the ABL can be quantified from the integrated buoyancy flux, plus possibly a small contribution from the shear production term near the surface, and compared to the total dissipation integrated throughout the ABL separately using all three wind component measurements to see which gives the best results. We also think that the longitudinal component is most likely to give correct dissipation measurements since it is less affected by flow distortion and has a long history of use on many aircraft in many
300 studies of atmospheric turbulence.

Code and data availability. The data used in this study were downloaded from the public datasets (Lothon and Brilouet, 2020; UCAR/NCAR - Earth Observing Laboratory, 2011a, b; Khelif, 2009). The MATLAB code we developed for the purpose of the presented analysis is available in the repository Nowak et al. (2024).

Appendix A: Segmentation algorithm

305 In order to select horizontal segments in RICO and POST flights (see sec. 2), we designed a simple algorithm which exploits the timeseries of altitude z, true heading ψ and TAS. The conditions are small derivatives of altitude dz/dx and true heading $d\psi/dx$ with respect to distance x as well as large TAS. The continuous flight legs where all samples meet those conditions constitute segments. From such a set of segments, we take only those exceeding the minimum length (specified below) and with a small overall altitude trend.

310 The C130 and TO differ in size, cruising speed and other airplane properties. Moreover, RICO flight strategy utilized large circles at constant altitude whereas POST utilized straight segments. Therefore, we separately adjusted the thresholds for those experiments. For C130 during RICO, we required: $4\,\mathrm{km}$ moving average of dz/dx smaller than $10\,\mathrm{m\,km^{-1}}$, $20\,\mathrm{km}$ moving average of $d\psi/dx$ smaller than $3\,^\circ\mathrm{km^{-1}}$, and segment length larger than $30\,\mathrm{km}$. For TO during POST, we required: $2\,\mathrm{km}$ moving average of dz/dx smaller than $12\,\mathrm{m\,km^{-1}}$, $2\,\mathrm{km}$ moving average of $d\psi/dx$ smaller than $5\,^\circ\mathrm{km^{-1}}$, and segment length

315 larger than $20\,\mathrm{km}$. In both cases, the minimum acceptable TAS was 0.9 of its flight median and the maximum acceptable altitude trend within the segment was $2\,\mathrm{m\,km^{-1}}$. An illustration of the segmentation algorithm applied to one of the RICO flights is given in Fig. A1.
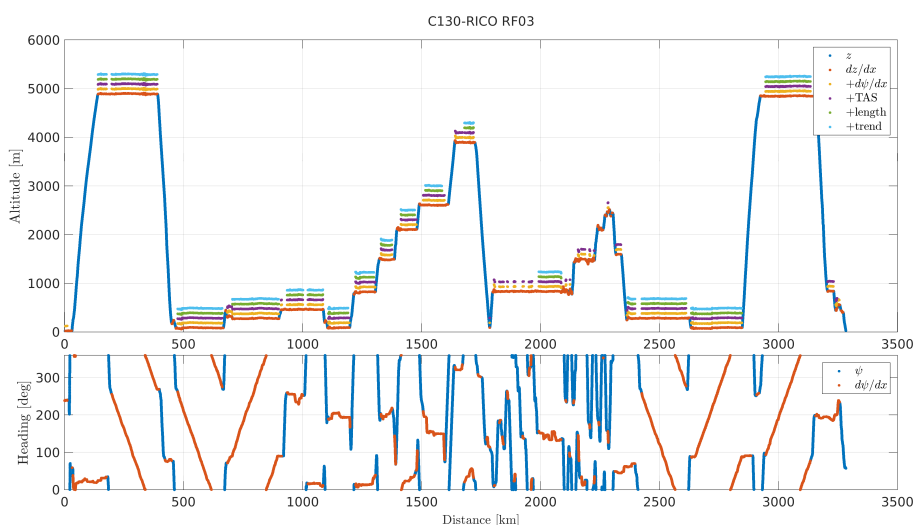

Figure A1. Segmentation algorithm applied to C130 RICO flight RF03. Upper panel: altitude (blue), sample points meeting the criteria of: small dz/dx (red), also small $d\psi/dx$ (yellow), also large TAS (purple), also large segment length (green), also small overall altitude trend (cyan). Lower panel: true heading (blue), samples meeting the criterion of small $d\psi/dx$ (red).

Appendix B: Uncertainties

We did not consider the errors for the individual instruments onboard research aircraft because the contributions to the final

320   measurement error related to the characteristics of the flow around the fuselage and the environmental conditions are often significant but hardly possible to quantify accurately. Instead, we evaluated the standard errors of the least-squares fits of the formulas in Eqs. (5), (6), (7) and (8). Those errors are indirectly affected by the integral length scale estimates which control the width of the fitting range.

The uncertainties in the presented results, i.e. the transverse-to-longitudinal ratios and scaling exponents, are obtained from

325   appropriately propagated errors originating from least-squares fits. We show their ranges in the form of box-and-whisker plots in Fig. B1. For the transverse-to-longitudinal ratios, the median values are below 0.2. In general, the lowest uncertainties are observed for EUREC4A while the highest for RICO and POST. The median uncertainties of s and p are below 0.05 and 0.1, respectively. Here, there is no clear tendency with respect to the experiment.
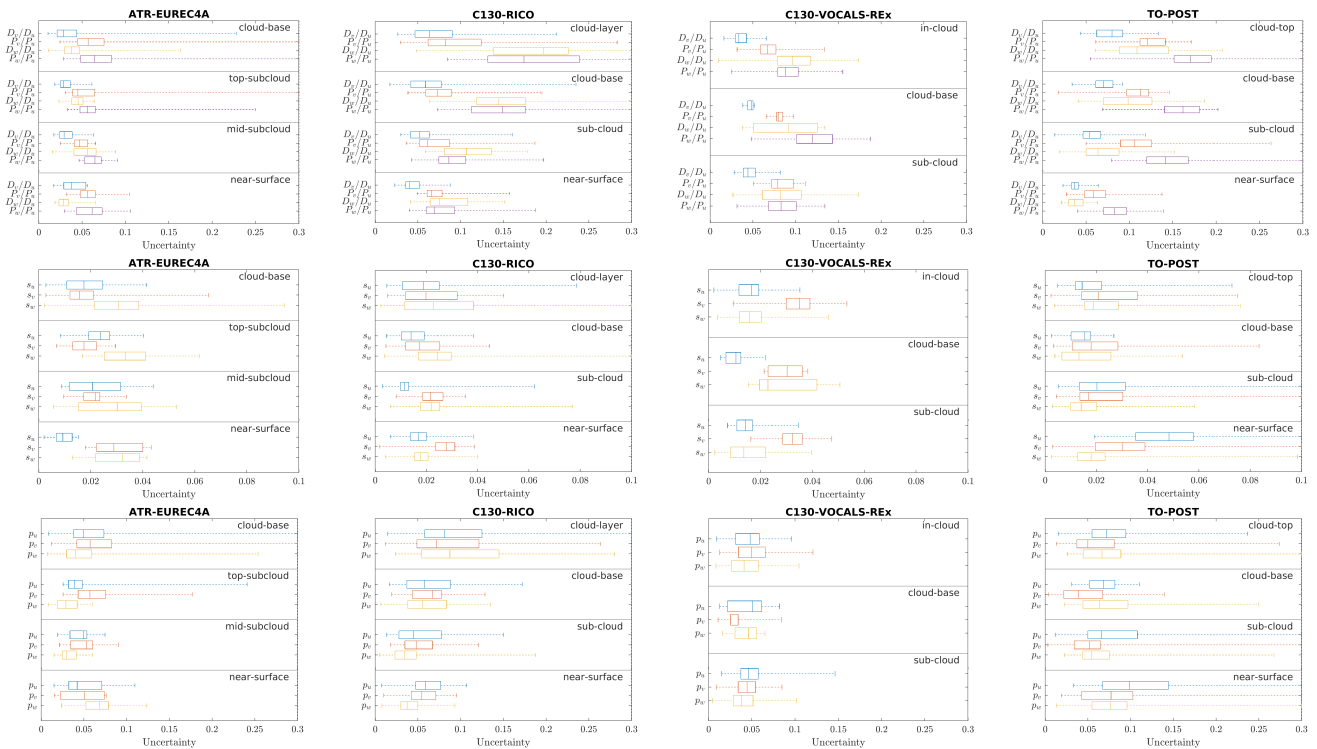
Figure B1. Uncertainties of the transverse-to-longitudinal ratios and scaling exponents for structure functions and power spectra in the form of box-and-whisker plots illustrating the range of values among segments belonging to each level in each experiment. The vertical line inside the box denotes the median value, box spans the interquartile range and whiskers span the entire range.

17

Appendix C: Sensitivity to fitting range

330   We examined the sensitivity of the results with respect to the choice of the fitting range by repeating the computations of the transverse-to-longitudinal ratios and the scaling exponents for six different values for the upper end of this range: from $0.6L$ to $1.4L$ separation distance in the case of structure functions and from $1.2L$ and $2.8L$ wavelength in the case of power spectra. The upper end for power spectra was twice as large as for structure functions in each such test. The other parameters, including the lower end of the fitting range, were kept the same as given in Sec. 3.

335   The results were not observed to change significantly with the fitting range. The plots as in Figs. 3, 4 and 5 are to a large extent similar regardless of the considered fitting range (not shown). In Fig. C1 we present the experiment-averaged results for each test. The variations related to the changes in the fitting range are typically smaller than between the experiments and negligible in comparison to the variability among individual segments visible in Figs. 3-5.
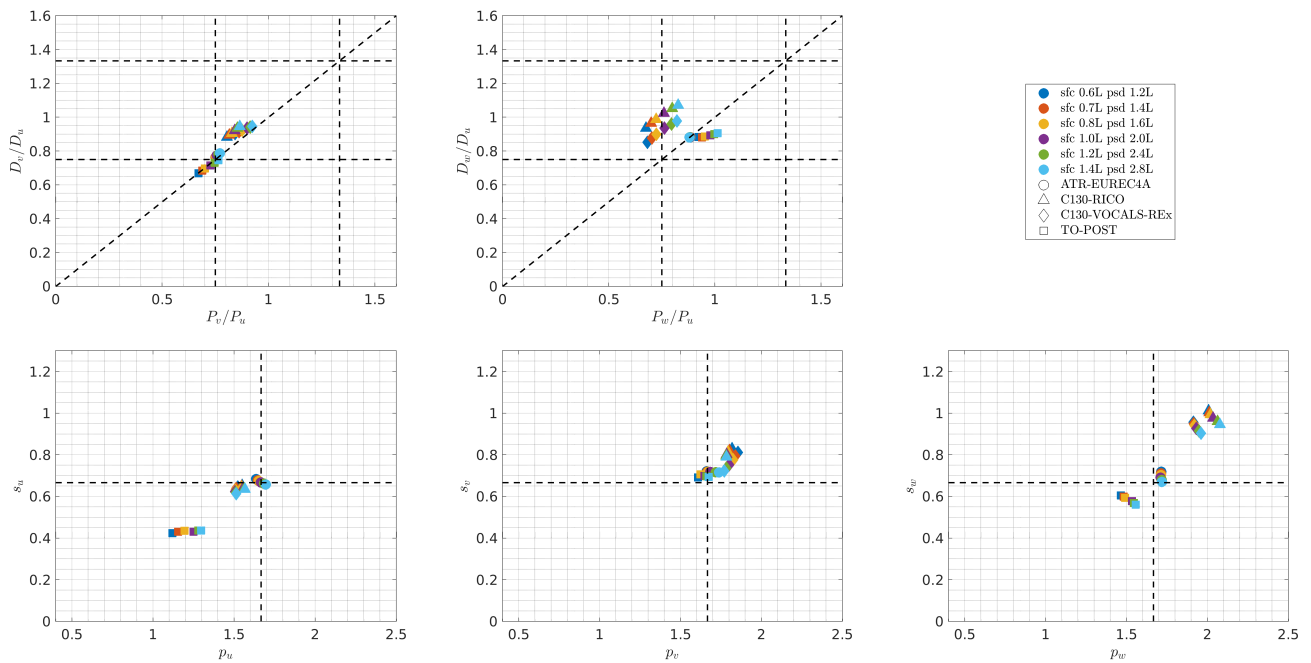

Figure C1. Experiment-averaged results on transverse-to-longitudinal ratios and scaling exponents obtained for the different widths of the fitting range. Colors denote the choices for the upper end of the fitting range for structure functions (sfc) and power spectra (psd); the lower end is the same as given in sec. 3. Different symbols denote the four experiments. The dashed black lines in the upper panels mark 4/3 and 3/4 values, and 1:1 proportion as in Figs. 3 and 4. In the lower panels, they mark the values of 2/3 and 5/3 as in Fig. 5.

References

Albright, A. L., Bony, S., Stevens, B., and Vogel, R.: Observed Subcloud-Layer Moisture and Heat Budgets in the Trades, Journal of the Atmospheric Sciences, 79, 2363–2385, https://doi.org/10.1175/JAS-D-21-0337.1, 2022.

Bony, S., Lothon, M., Delanoë, J., Coutris, P., Etienne, J. C., Aemisegger, F., Albright, A. L., André, T., Bellec, H., Baron, A., Bourdinot,
350 J. F., Brilouet, P. E., Bourdon, A., Canonici, J. C., Caudoux, C., Chazette, P., Cluzeau, M., Cornet, C., Desbios, J. P., Duchanoy, D., Flamant, C., Fildier, B., Gourbeyre, C., Guiraud, L., Jiang, T., Lainard, C., Le Gac, C., Lendroit, C., Lernould, J., Perrin, T., Pouvesle, F., Richard, P., Rochetin, N., Salaün, K., Schwarzenboeck, A., Seurat, G., Stevens, B., Totems, J., Touzé-Peiffer, L., Vergez, G., Vial, J., Villiger, L., and Vogel, R.: EUREC4A observations from the SAFIRE ATR42 aircraft, Earth System Science Data, 14, 2021–2064, https://doi.org/10.5194/ESSD-14-2021-2022, 2022.

355 Brilouet, P. E., Lothon, M., Etienne, J. C., Richard, P., Bony, S., Lernoult, J., Bellec, H., Vergez, G., Perrin, T., Delanoë, J., Jiang, T., Pouvesle, F., Lainard, C., Cluzeau, M., Guiraud, L., Medina, P., and Charoy, T.: The EUREC4A turbulence dataset derived from the SAFIRE ATR 42 aircraft, Earth System Science Data, 13, 3379–3398, https://doi.org/10.5194/ESSD-13-3379-2021, 2021.

Brown, E. N., Friehe, C. A., and Lenschow, D. H.: The Use of Pressure Fluctuations on the Nose of an Aircraft for Measuring Air Motion, Journal of Applied Meteorology and Climatology, 22, 171–180, https://doi.org/10.1175/1520-0450(1983)022<0171:TUOPFO>2.0.CO;2,
360 1983.

Carman, J. K., Rossiter, D. L., Khelif, D., Jonsson, H. H., Faloona, I. C., and Chuang, P. Y.: Observational constraints on entrainment and the entrainment interface layer in stratocumulus, Atmospheric Chemistry and Physics, 12, 11135–11152, https://doi.org/10.5194/ACP-12-11135-2012, 2012.

Chamecki, M. and Dias, N. L.: The local isotropy hypothesis and the turbulent kinetic energy dissipation rate in the atmospheric surface
365 layer, Quarterly Journal of the Royal Meteorological Society, 130, 2733–2752, https://doi.org/10.1256/QJ.03.155, 2004.

Darbieu, C., Lohou, F., Lothon, M., Vilà-Guerau De Arellano, J., Couvreux, F., Durand, P., Pino, D., Patton, E. G., Nilsson, E., Blay-Carreras, E., and Gioli, B.: Turbulence vertical structure of the boundary layer during the afternoon transition, Atmospheric Chemistry and Physics, 15, 10071–10086, https://doi.org/10.5194/ACP-15-10071-2015, 2015.

Duynkerke, P. G., Heqing Zhang, and Jonker, P. J.: Microphysical and turbulent structure of nocturnal stratocumulus as observed during
370 ASTEX, Journal of the Atmospheric Sciences, 52, 2763–2777, https://doi.org/10.1175/1520-0469(1995)052<2763:MATSON>2.0.CO;2, 1995.

Earth Observing Laboratory: NSF/NCAR C-130, https://doi.org/10.5065/D6WM1BG0.

Faloona, I., Lenschow, D. H., Campos, T., Stevens, B., van Zanten, M., Blomquist, B., Thornton, D., Bandy, A., and Gerber, H.: Observations of entrainment in eastern Pacific marine stratocumulus using three conserved scalars, Journal of the Atmospheric Sciences, 62, 3268–3285,
375 https://doi.org/10.1175/JAS3541.1, 2005.

Gerber, H., Frick, G., Malinowski, S. P., Jonsson, H., Khelif, D., and Krueger, S. K.: Entrainment rates and microphysics in POST stratocumulus, Journal of Geophysical Research Atmospheres, 118, 12,094–12,109, https://doi.org/10.1002/JGRD.50878, 2013.

Gomes-Fernandes, R., Ganapathisubramani, B., and Vassilicos, J. C.: The energy cascade in near-field non-homogeneous non-isotropic turbulence, Journal of Fluid Mechanics, 771, 676–705, https://doi.org/10.1017/JFM.2015.201, 2015.

380 Grabowski, W. W. and Wang, L.-P.: Growth of Cloud Droplets in a Turbulent Environment, Annual Review of Fluid Mechanics, 45, 293–324, https://doi.org/10.1146/annurev-fluid-011212-140750, 2013.

Jen-La Plante, I., Ma, Y., Nurowska, K., Gerber, H., Khelif, D., Karpinska, K., Kopec, M. K., Kumala, W., and Malinowski, S. P.: Physics of stratocumulus top (POST): turbulence characteristics, Atmos. Chem. Phys., 16, 9711–9725, https://doi.org/10.5194/acp-16-9711-2016, 2016.

385 Kaimal, J. C., Wyngaard, J. C., Izumi, Y., and Coté, O. R.: Spectral characteristics of surface-layer turbulence, Quarterly Journal of the Royal Meteorological Society, 98, 563–589, https://doi.org/10.1002/QJ.49709841707, 1972.

Khelif, D.: POST: UC Irvine 40-hz Probes - netCDF format. Version 1.0., https://doi.org/10.26023/KP56-KFJS-VC07, 2009.

Kolmogorov, A. N.: The local structure of turbulence in incompressible viscous fluid for very large Reynolds numbers, Dokl. Akad. Nauk SSSR, 30, 301–304, https://doi.org/10.1098/rspa.1991.0075, 1941.

390 Lambert, D. and Durand, P.: The marine atmospheric boundary layer during semaphore. I: Mean vertical structure and non-axisymmetry of turbulence, Quarterly Journal of the Royal Meteorological Society, 125, 495–512, https://doi.org/10.1002/qj.49712555407, 1999.

Lenschow, D. H.: Model of the Height Variation of the Turbulence Kinetic Energy Budget in the Unstable Planetary Boundary Layer, Journal of the Atmospheric Sciences, 31, 465–474, https://doi.org/10.1175/1520-0469(1974)031<0465:MOTHVO>2.0.CO;2, 1974.

Lenschow, D. H.: Aircraft Measurements in the Boundary Layer, in: Probing the Atmospheric Boundary Layer, pp. 39–55, American Mete-
395 orological Society, Boston, MA, ISBN 978-1-944970-14-7, https://doi.org/10.1007/978-1-944970-14-7_5, 1986.

Lenschow, D. H. and Spyers-Duran, P.: Air motion sensing, in: RAF Bulletin 23: Measurement techniques, University Corporation for Atmospheric Research, 1989.

Lenschow, D. H., Friehe, C. A., and Larue, J. C.: The development of an airborne hot-wire anemometer system, in: Fourth Symp. on Meteorological Observations and Instrumentation, vol. 24, pp. 463–466, American Meteorological Society, Denver, 1978.

400 Lenschow, D. H., Mann, J., and Kristensen, L.: How long is long enough when measuring fluxes and other turbulence statistics?, Journal of Atmospheric and Oceanic Technology, 11, 661–673, https://doi.org/10.1175/1520-0426(1994)011<0661:HLILEW>2.0.CO;2, 1994.

Lenschow, D. H., Zhou, M., Zeng, X., Chen, L., and Xu, X.: Measurements of fine-scale structure at the top of marine stratocumulus, Boundary-Layer Meteorology, 97, 331–357, https://doi.org/10.1023/A:1002780019748, 2000.

Leon, D., Zuidema, P., and Leon, D.: VOCALS: NSF/NCAR C130 Radar, Lidar and Radiometer Integrated Dataset. Version 1.0.,
405 https://doi.org/10.26023/8KEJ-BQNG-W808, 2011.

Lothon, M. and Brilouet, P.: SAFIRE ATR42: Turbulence Data 25 Hz, https://doi.org/10.25326/128, 2020.

Lothon, M. and Lenschow, D.: Status report on C-130 air-motion measurements, Tech. rep., https://archive.eol.ucar.edu/raf/Projects/DYCOMS-II/DYCOMSII.issues.pdf, 2005a.

Lothon, M. and Lenschow, D.: Status-reminder report on C-130 air-motion measurements: Test of DYCOMS-II new datasets, Tech. rep.,
410 https://archive.eol.ucar.edu/raf/Projects/DYCOMS-II/DYCOMS.report1_win07.pdf, 2007.

Lothon, M. and Lenschow, D. H.: Report on C-130 air-motion measurements: Spectra of the air velocity components, Tech. rep., 2005b.

Malinowski, S. P., Gerber, H., Jen-La Plante, I., Kopec, M. K., Kumala, W., Nurowska, K., Chuang, P. Y., Khelif, D., and Haman, K. E.: Physics of stratocumulus top (POST): turbulent mixing across capping inversion, Atmos.Chem.and Phys., 13, 12 171–12 186, https://doi.org/10.5194/acp-13-12171-2013, 2013.

415 Mauritsen, T., Svensson, G., Zilitinkevich, S. S., Esau, I., Enger, L., and Grisogono, B.: A Total Turbulent Energy Closure Model for Neutrally and Stably Stratified Atmospheric Boundary Layers, Journal of the Atmospheric Sciences, 64, 4113–4126, https://doi.org/https://doi.org/10.1175/2007JAS2294.1, 2007.

Merceret, F. J.: Airborne Hot-Film Measurements of the Small-Scale Structure of Atmospheric Turbulence During GATE, Journal of the Atmospheric Sciences, 33, 1739–1746, https://doi.org/10.1175/1520-0469(1976)033, 1976a.

420 Merceret, F. J.: Measuring Atmospheric Turbulence with Airborne Hot-Film Anemometers, Journal of Applied Meteorology and Climatology, 15, 482–490, https://doi.org/10.1175/1520-0450(1976)015<0482:MATWAH>2.0.CO;2, 1976b.

NASA Airborne Science Program: Twin Otter - CIRPAS - NPS, https://airbornescience.nasa.gov/aircraft/Twin_Otter_-_CIRPAS_-_NPS.

Nicholls, S.: The dynamics of stratocumulus: Aircraft observations and comparisons with a mixed layer model, Quarterly Journal of the Royal Meteorological Society, 110, 783–820, https://doi.org/10.1002/qj.49711046603, 1984.

425 Nicholls, S. and Leighton, J.: An observational study of the structure of stratiform cloud sheets: Part I. Structure, Quarterly Journal of the Royal Meteorological Society, 112, 431–460, https://doi.org/10.1002/qj.49711247209, 1986.

Nowak, J. L., Siebert, H., Szodry, K. E., and Malinowski, S. P.: Coupled and decoupled stratocumulus-topped boundary layers: Turbulence properties, Atmospheric Chemistry and Physics, 21, 10 965–10 991, https://doi.org/10.5194/ACP-21-10965-2021, 2021.

Nowak, J. L., Lothon, M., Lenschow, D. H., and Malinowski, S. P.: The ratio of transverse to longitudinal turbulent velocity statistics for
430 aircraft measurements: software, https://doi.org/10.5281/zenodo.11127723, 2024.

Pedersen, J. G., Ma, Y. F., Grabowski, W. W., and Malinowski, S. P.: Anisotropy of observed and simulated turbulence in marine stratocumulus, J. Adv. Model. Earth Syst., 10, 500–515, https://doi.org/10.1002/2017ms001140, 2018.

Pope, S. B.: Turbulent flows, Cambridge University Press, Cambridge, ISBN 9780521598866, https://doi.org/10.1017/CBO9780511840531, 2000.

435 Rauber, R. M., Stevens, B., Ochs, H. T., Knight, C., Albrecht, B. A., Blyth, A. M., Fairall, C. W., Jensen, J. B., Lasher-Trapp, S. G., Mayol-Bracero, O. L., Vali, G., Anderson, J. R., Baker, B. A., Bandy, A. R., Burnet, E., Brenguier, J.-L., Brewer, W. A., Brown, P. R. A., Chuang, P., Cotton, W. R., Girolamo, L. D., Geerts, B., Gerber, H., Göke, S., Gomes, L., Heikes, B. G., Hudson, H. G., Kollias, P., Lawson, R. P., Krueger, S. K., Lenschow, D. H., Nuijens, L., O'sullivan, D. W., Rilling, R. A., Rogers, D. C., Siebesma, A. P., Snodgrass, E., Stith, J. L., Thornton, D. C., Tucker, S., Twohy, C. H., Zuidema, P., Rauber, R. M., Ochs Iii, H. T., and Di Girolamo, L.: A Supplement
440 to Rain in Shallow Cumulus Over the Ocean: The RICO Campaign, Bulletin of the American Meteorological Society, 88, S12–S18, https://doi.org/10.1175/BAMS-88-12-RAUBER, 2007a.

Rauber, R. M., Stevens, B., Ochs, H. T., Knight, C., Albrecht, B. A., Blythe, A. M., Fairall, C. W., Jensen, J. B., Lasher-Trapp, S. G., Mayol-Bracero, O. L., Vali, G., Anderson, J. R., Baker, B. A., Bandy, A. R., Brunet, E., Brenguier, J. L., Brewer, W. A., Brown, P. R., Chuang, P., Cotton, W. R., Di Girolamo, L., Geerts, B., Gerber, H., Göke, S., Gomes, L., Heikes, B. G., Hudson, J. G., Kollias, P., Lawson, R. P.,
445 Krueger, S. K., Lenschow, D. H., Nuijens, L., O'Sullivan, D. W., Rilling, R. A., Rogers, D. C., Siebesma, A. P., Snodgrass, F., Stith, J. L., Thornton, D. C., Tucker, S., Twohy, C. H., and Zuidema, P.: Rain in Shallow Cumulus Over the Ocean: The RICO Campaign, Bulletin of the American Meteorological Society, 88, 1912–1928, https://doi.org/10.1175/BAMS-88-12-1912, 2007b.

Raymond, D. J., Esbensen, S. K., Paulson, C., Gregg, M., Bretherton, C. S., Petersen, W. A., Cifelli, R., Shay, L. K., Ohlmann, C., and Zuidema, P.: EPIC2001 and the Coupled Ocean–Atmosphere System of the Tropical East Pacific, Bulletin of the American Meteorological
450 Society, 85, 1341–1354, https://doi.org/10.1175/BAMS-85-9-1341, 2004.

Romero, L. and Melville, W. K.: Airborne Observations of Fetch-Limited Waves in the Gulf of Tehuantepec, Journal of Physical Oceanography, 40, 441–465, https://doi.org/10.1175/2009JPO4127.1, 2010.

Saddoughi, S. G. and Veeravalli, S. V.: Local isotropy in turbulent boundary layers at high Reynolds number, Journal of Fluid Mechanics, 268, 333–372, https://doi.org/10.1017/S0022112094001370, 1994.

455 SAFIRE: The SAFIRE ATR42 offers a big scientific payload, https://www.safire.fr/en/content_page/safire-utilisateurs/latr42-2.html.

Sheih, C. M., Tennekes, H., and Lumley, J. L.: Airborne Hot-Wire Measurements of the Small-Scale Structure of Atmospheric Turbulence, The Physics of Fluids, 14, 201–215, https://doi.org/10.1063/1.1693416, 1971.

Siebert, H. and Muschinski, A.: Relevance of a tuning-fork effect for temperature measurements with the Gill solent HS ultrasonic anemometer-thermometer, Journal of Atmospheric and Oceanic Technology, 18, 1367–1376, https://doi.org/10.1175/1520-
460   0426(2001)018<1367:ROATFE>2.0.CO;2, 2001.

Siebert, H., Franke, H., Lehmann, K., Maser, R., Saw, E. W., Schell, D., Shaw, R. A., and Wendisch, M.: Probing finescale dynamics and microphysics of clouds with helicopter-borne measurements, Bulletin of the American Meteorological Society, 87, 1727–1738, https://doi.org/10.1175/BAMS-87-12-1727, 2006a.

Siebert, H., Lehmann, K., and Wendisch, M.: Observations of small-scale turbulence and energy dissipation rates in the cloudy boundary
465   layer, Journal of the Atmospheric Sciences, 63, 1451–1466, https://doi.org/10.1175/JAS3687.1, 2006b.

Siebert, H., Lehmann, K., and Shaw, R. A.: On the use of hot-wire anemometers for turbulence measurements in clouds, Journal of Atmospheric and Oceanic Technology, 24, 980–993, https://doi.org/10.1175/JTECH2018.1, 2007.

Sreenivasan, K. R.: On the universality of the Kolmogorov constant, Physics of Fluids, 7, 2778–2784, https://doi.org/10.1063/1.868656, 1995.

470   Stevens, B., Lenschow, D. H., Vali, G., Gerber, H., Bandy, A., Blomquist, B., Brenguier, J. L., Bretherton, C. S., Burnet, F., Campos, T., Chai, S., Faloona, I., Friesen, D., Haimov, S., Laursen, K., Lilly, D. K., Loehrer, S. M., Malinowski, S. P., Morley, B., Petters, M. D., Rogers, D. C., Russell, L., Savic-Jovcic, V., Snider, J. R., Straub, D., Szumowski, M. J., Takagi, H., Thornton, D. C., Tschudi, M., Twohy, C., Wetzel, M., and Van Zanten, M. C.: Dynamics and Chemistry of Marine Stratocumulus—DYCOMS-II, Bulletin of the American Meteorological Society, 84, 579–594, https://doi.org/10.1175/BAMS-84-5-579, 2003.

475   Stevens, B., Bony, S., Farrell, D., Ament, F., Blyth, A., Fairall, C., Karstensen, J., Quinn, P. K., Speich, S., Acquistapace, C., Aemisegger, F., Albright, A. L., Bellenger, H., Bodenschatz, E., Caesar, K. A., Chewitt-Lucas, R., De Boer, G., Delanoë, J., Denby, L., Ewald, F., Fildier, B., Forde, M., George, G., Gross, S., Hagen, M., Hausold, A., Heywood, K. J., Hirsch, L., Jacob, M., Jansen, F., Kinne, S., Klocke, D., Kölling, T., Konow, H., Lothon, M., Mohr, W., Naumann, A. K., Nuijens, L., Olivier, L., Pincus, R., Pöhlker, M., Reverdin, G., Roberts, G., Schnitt, S., Schulz, H., Pier Siebesma, A., Stephan, C. C., Sullivan, P., Touzé-Peiffer, L., Vial, J., Vogel, R., Zuidema,
480   P., Alexander, N., Alves, L., Arixi, S., Asmath, H., Bagheri, G., Baier, K., Bailey, A., Baranowski, D., Baron, A., Barrau, S., Barrett, P. A., Batier, F., Behrendt, A., Bendinger, A., Beucher, F., Bigorre, S., Blades, E., Blossey, P., Bock, O., Böing, S., Bosser, P., Bourras, D., Bouruet-Aubertot, P., Bower, K., Branellec, P., Branger, H., Brennek, M., Brewer, A., Brilouet, P. E., Brügmann, B., Buehler, S. A., Burke, E., Burton, R., Calmer, R., Canonici, J. C., Carton, X., Cato, G., Charles, J. A., Chazette, P., Chen, Y., Chilinski, M. T., Choularton, T., Chuang, P., Clarke, S., Coe, H., Cornet, C., Coutris, P., Couvreux, F., Crewell, S., Cronin, T., Cui, Z., Cuypers, Y., Daley, A., Damerell,
485   G. M., Dauhut, T., Deneke, H., Desbios, J. P., Dörner, S., Donner, S., Douet, V., Drushka, K., Dütsch, M., Ehrlich, A., Emanuel, K., Emmanouilidis, A., Etienne, J. C., Etienne-Leblanc, S., Faure, G., Feingold, G., Ferrero, L., Fix, A., Flamant, C., Flatau, P. J., Foltz, G. R., Forster, L., Furtuna, I., Gadian, A., Galewsky, J., Gallagher, M., Gallimore, P., Gaston, C., Gentemann, C., Geyskens, N., Giez, A., Gollop, J., Gouirand, I., Gourbeyre, C., De Graaf, D., De Groot, G. E., Grosz, R., Güttler, J., Gutleben, M., Hall, K., Harris, G., Helfer, K. C., Henze, D., Herbert, C., Holanda, B., Ibanez-Landeta, A., Intrieri, J., Iyer, S., Julien, F., Kalesse, H., Kazil, J., Kellman, A., Kidane, A. T.,
490   Kirchner, U., Klingebiel, M., Körner, M., Kremper, L. A., Kretzschmar, J., Krüger, O., Kumala, W., Kurz, A., L'Hégaret, P., Labaste, M., Lachlan-Cope, T., Laing, A., Landschützer, P., Lang, T., Lange, D., Lange, I., Laplace, C., Lavik, G., Laxenaire, R., LeBihan, C., Leandro, M., Lefevre, N., Lena, M., Lenschow, D., Li, Q., Lloyd, G., Los, S., Losi, N., Lovell, O., Luneau, C., Makuch, P., Malinowski, S., Manta, G., Marinou, E., Marsden, N., Masson, S., Maury, N., Mayer, B., Mayers-Als, M., Mazel, C., McGeary, W., McWilliams, J. C., Mech, M., Mehlmann, M., Meroni, A. N., Mieslinger, T., Minikin, A., Minnett, P., Möller, G., Avalos, Y. M., Muller, C., Musat,
495   I., Napoli, A., Neuberger, A., Noisel, C., Noone, D., Nordsiek, F., Nowak, J. L., Oswald, L., Parker, D. J., Peck, C., Person, R., Philippi,

M., Plueddemann, A., Pöhlker, C., Pörtge, V., Pöschl, U., Pologne, L., Posyniak, M., Prange, M., Meléndez, E. Q., Radtke, J., Ramage, K., Reimann, J., Renault, L., Reus, K., Reyes, A., Ribbe, J., Ringel, M., Ritschel, M., Rocha, C. B., Rochetin, N., Röttenbacher, J., Rollo, C., Royer, H., Sadoulet, P., Saffin, L., Sandiford, S., Sandu, I., Schäfer, M., Schemann, V., Schirmacher, I., Schlenczek, O., Schmidt, J., Schröder, M., Schwarzenboeck, A., Sealy, A., Senff, C. J., Serikov, I., Shohan, S., Siddle, E., Smirnov, A., Späth, F., Spooner, B.,

500   Katharina Stolla, M., Szkólka, W., De Szoeke, S. P., Tarot, S., Tetoni, E., Thompson, E., Thomson, J., Tomassini, L., Totems, J., Ubele, A. A., Villiger, L., Von Arx, J., Wagner, T., Walther, A., Webber, B., Wendisch, M., Whitehall, S., Wiltshire, A., Wing, A. A., Wirth, M., Wiskandt, J., Wolf, K., Worbes, L., Wright, E., Wulfmeyer, V., Young, S., Zhang, C., Zhang, D., Ziemen, F., Zinner, T., and Zöger, M.: EUREC4A, Earth System Science Data, 13, 4067–4119, https://doi.org/10.5194/ESSD-13-4067-2021, 2021.

Stith, J. and Rogers, D. C.: Instrument development and education in airborne science, in: 13th Symposium on Education, 84th AMS Annual
505   Meeting, Seattle, 2004.

Stull, R. B.: An Introduction to Boundary Layer Meteorology, Springer Netherlands, Dordrecht, ISBN 978-90-277-2769-5, https://doi.org/10.1007/978-94-009-3027-8, 1988.

Tjernström, M. and Rogers, D. P.: Turbulence structure in decoupled marine stratocumulus: A case study from the ASTEX field experiment, Journal of the Atmospheric Sciences, 53, 598–619, https://doi.org/10.1175/1520-0469(1996)053<0598:TSIDMS>2.0.CO;2, 1996.

510   UCAR/NCAR - Earth Observing Laboratory: NCAR/NSF C-130 Navigation, State Parameter, and Microphysics HRT Data - 25 Hz. Version 1.0., https://doi.org/10.5065/D64J0CDM, 2011a.

UCAR/NCAR - Earth Observing Laboratory: NCAR/NSF C-130 Navigation, State Parameter, and Microphysics HRT (25 sps) Data. Version 1.0., https://doi.org/10.5065/D69K48JK, 2011b.

Wacławczyk, M., Gozingan, A. S., Nzotungishaka, J., Mohammadi, M., and P. Malinowski, S.: Comparison of Different Techniques to Cal-
515   culate Properties of Atmospheric Turbulence from Low-Resolution Data, Atmosphere, 11, 199, https://doi.org/10.3390/atmos11020199, 2020.

Wacławczyk, M., Nowak, J. L., Siebert, H., and Malinowski, S. P.: Detecting Nonequilibrium States in Atmospheric Turbulence, Journal of the Atmospheric Sciences, 79, 2757–2772, https://doi.org/10.1175/JAS-D-22-0028.1, 2022.

Welch, P. D.: The Use of Fast Fourier Transform for the Estimation of Power Spectra: A Method Based on Time Averaging Over Short,
520   Modified Periodograms, IEEE Transactions on Audio and Electroacoustics, 15, 70–73, https://doi.org/10.1109/TAU.1967.1161901, 1967.

Wendisch, M. and Brenguier, J. L.: Airborne Measurements for Environmental Research, Wiley-VCH Verlag GmbH and Co. KGaA, Weinheim, Germany, ISBN 9783527653218, https://doi.org/10.1002/9783527653218, 2013.

Wood, R., Mechoso, C. R., Bretherton, C. S., Weller, R. A., Huebert, B., Straneo, F., Albrecht, B. A., Coe, H., Allen, G., Vaughan, G., Daum, P., Fairall, C., Chand, D., Gallardo Klenner, L., Garreaud, R., Grados, C., Covert, D. S., Bates, T. S., Krejci, R., Russell, L. M.,
525   De Szoeke, S., Brewer, A., Yuter, S. E., Springston, S. R., Chaigneau, A., Toniazzo, T., Minnis, P., Palikonda, R., Abel, S. J., Brown, W. O., Williams, S., Fochesatto, J., Brioude, J., and Bower, K. N.: The VAMOS ocean-cloud-atmosphere-land study regional experiment (VOCALS-REx): Goals, platforms, and field operations, Atmospheric Chemistry and Physics, 11, 627–654, https://doi.org/10.5194/ACP-11-627-2011, 2011.

Zheng, X., Albrecht, B., Jonsson, H. H., Khelif, D., Feingold, G., Minnis, P., Ayers, K., Chuang, P., Donaher, S., Rossiter, D., Ghate, V., Ruiz-
530   Plancarte, J., and Sun-Mack, S.: Observations of the boundary layer, cloud, and aerosol variability in the southeast Pacific near-coastal marine stratocumulus during VOCALS-REx, Atmospheric Chemistry and Physics, 11, 9943–9959, https://doi.org/10.5194/ACP-11-9943-2011, 2011.